1   **A physically-based distributed karst hydrological model (QMG**

2   **model-V1.0) for flood simulations**

3   **Ji Li[1,*], Daoxian Yuan[1,2], Fuxi Zhang[3], Yongjun Jiang[1], Jiao Liu[4], Mingguo Ma[1]**

4   [1]Chongqing Jinfo Mountain Karst Ecosystem National Observation and Research

5   Station，Chongqing Key Laboratory of Karst Environment, School of Geographical

6   Sciences, Southwest University, Chongqing 400715, China

7   [2]Karst Dynamic Laboratory, Ministry of Land and Resources, Guilin 541004, China

8   [3]College of Engineering Science and Technology, Shanghai Ocean University;

9   Shanghai Engineering Research Center of Marine Renewable Energy 201306, China

10   [4]Chongqing municipal hydrological monitoring station, Chongqing 401120, China

11   Corresponding author: Ji Li (445776649@qq.com)

12   **Abstract** Karst trough valleys are prone to flooding, primarily because of the unique

13   hydrogeological features of karst landform, which are conducive to the spread of rapid

14   runoff. Hydrological models that represent the complicated hydrological processes in karst

15   regions are effective for predicting karst flooding, but their application has been hampered

16   by their complex model structures and associated parameter set, especially so for distributed

17   hydrological models, which require large amounts of hydrogeological data. Distributed

18   hydrological models for predicting the ~~Karst~~ flooding is highly dependent on distributed

19   ~~structrues~~ modeling, complicated boundary parameters setting, and tremendous

20   hydrogeological data processing that is both time and computational power consuming.

21   Proposed here is a distributed physically-based karst hydrological model, known as the

22   QMG (Qingmuguan) model. The structural design of this model is relatively simple, and it is

23 generally divided into surface and underground double-layered structures. The parameters

24 that represent the structural functions of each layer have clear physical meanings, and the

25 parameters are less than those of the current distributed models. This allows modeling in

26 karst areas with only a small amount of necessary hydrogeological data. 18 flood processes

27 across the karst underground river in the Qingmuguan karst trough valley are simulated by

28 the QMG model, and the simulated values agree well with observations, for which the

29 average value of Nash–Sutcliffe coefficient was 0.92. A sensitivity analysis shows that the

30 infiltration coefficient, permeability coefficient, and rock porosity are the parameters that

31 require the most attention in model calibration and optimization. The improved

32 predictability of karst flooding by the proposed QMG model promotes a better mechanistic

33 depicting of runoff generation and confluence in karst trough valleys.

34 **Keywords:** Simulation and forecasting of karst floods; Karst trough valleys; QMG

35 (Qingmuguan) model; Parametric optimization; Parameter sensitivity analysis

36 **1. Introduction**

37 Karst trough valleys are very common in China, especially in the southwest. In general,

38 these karst areas are water scarce because their surfaces store very little rainfall, but it is also

39 a protential birthplace for floods. Because trough and valley landforms and topographic

40 features facilitate the formation and propagation of floods (Li et al., 2021). Taking the study

41 area, the Qingmuguan karst trough valley for example, floods used to happen here

42 constantly. In recent years, with the increase in extreme rainfall events and the increased

43 area of construction land in the region, rainfall infiltration decreased as long as rapid runoff

44 over impervious surfaces increased that results in frequent catastrophic flooding in the basin

45 (Liu et al., 2009). Excess water overflows from karst sinkholes and underground river

46 outlets often occur during floods, flooding large areas of farmland and residential areas and

47 causing serious economic losses (Yu et al., 2020). Therefore, the simulation and prediction

48 of karst flooding events in these karst trough valleys like the study area are both important

49 and urgently needed.

50   Hydrological models can be effective for forecasting floods and evaluating water

51 resources in karst areas (Ford and Williams, 2007; Williams, 2009). However, modeling

52 floods in karst regions is extremely difficult because of the complex hydrogeological

53 structure. Karst water-bearing systems consist of multiple media under the influence of

54 complex karst development dynamics (Worthington et al., 2000; Kovács and Perrochet,

55 2008), such as karst caves, conduits, fissures and pores, and are usually highly spatially

56 heterogeneous (Chang and Liu, 2015; Mario et al., 2019). In addition, the intricate surface

57 hydrogeological conditions and the hydrodynamic conditions inside the karst water-bearing

58 medium result in significant temporal and spatial differences in the hydrological processes in

59 karst areas (Geyer et al., 2008; Bittner et al., 2020).

60   Early studies on flood forecasting in karst regions, with simplified lumped hydrological

61 models, were commonly used to describe the rainfall–discharge relationship (e.g., Kovács

62 and Sauter, 2007; Fleury et al., 2007b; Jukić and Denić, 2009; Hartmann et al., 2014a). With

63 the development of physical exploration technology and the progress made in mathematics,

64 computing, and other interdisciplinary disciplines, the level of modeling has gradually

65 improved (Hartmann and Baker, 2017; Hartmann, 2018; Petrie et al., 2021). Distributed

66 hydrological models have subsequently become widely used in karst areas. The main

67 difference between the lumped and distributed hydrological models is that the latter divide

68 the entire basin into many sub-basins to calculate the runoff generation and confluence,

69 thereby better describing the physical properties of the hydrological processes inside the

70 karst water-bearing system (Hartmann, 2018; Epting et al., 2018).

71   Because of their simple structure and little demand for modeling data, lumped

72 hydrological models have been used widely in karst areas (Kurtulus and Razack, 2007;

73 Ladouche et al., 2014). In a lumped model, the river basin is considered as a whole to

74 calculate the runoff generation and confluence, and there is no division running into

75 sub-basins (Dewandel et al., 2003; Bittner et al., 2020). Lumped models usually consider the

76 inputs and outputs of the model (Liedl and Sauter, 2003; Hartmann and Bake, 2013, 2017).

77   In addition, most of the model parameters are not optimized in a lumped model, and the

78   physical meaning of each parameter is unclear (Chen, 2009; Bittner et al., 2020).

79   Distributed hydrological models are of active interest in flood simulation and

80   forecasting research (Ambroise et al., 1996; Beven and Binley, 2006; Zhu and Li, 2014).

81   Compared with a lumped model, a distributed model has a more definite physical

82   significance for the model structure in terms of its mechanism (Meng and Wang, 2010;

83   Epting et al., 2018). In a distributed hydrological model, an entire karst basin can be divided

84   into many sub-basins (Birk et al., 2005) using high-resolution digital elevation map (DEM)

85   data. In the rainfall-runoff algorithm of the model, the hydrogeological conditions and karst

86   aquifer characteristics can be fully considered to precisely simulate the runoff generation

87   and confluence (Gang et al., 2019). The commonly used basin distributed hydrological

88   models (i.e., not a special groundwater numerical model such as MODFLOW) have also

89   been applied widely in karst areas, and include the SHE/MIKE SHE model (Abbott et al.,

90   1986a,b; Doummar et al., 2012), SWMM model (Peterson and Wicks, 2006; Blansett and

91   Hamlett, 2010; Blansett, 2011), TOPMODEL (Ambroise et al., 1996; Suo et al., 2007; Lu

92   et al., 2013; Pan, 2014), and SWAT model (Peterson and Hamlett, 1998; Ren, 2006).

93   The commonly used distributed hydrological models have multiple structures and

94   numerous parameters (Lu et al., 2013; Pan, 2014), which make distributed model may need

95   vast amounts of data to build its framework in karst regions. For example, the distributed

96   groundwater model MODFLOW-CFPM1 requires detailed data regarding the distribution of

97   karst conduits in a study area (Reimann et al., 2009; Qin and Jiang, 2014). Another example

98   is the Karst–Liuxihe model (Li et al., 2019), which has 5 underground vertical layers in the

99   model structure and has 15 parameters, make it hard to model in karst areas. In addition, a

100 special borehole pumping test may be required to obtain the rock permeability coefficient.

101   To overcome the difficulty of the large modeling-data demands for distributed

102 hydrological models in karst areas, a new physical model based on distributed hydrological

103 known as the QMG (Qingmuguan) model was developed. This QMG model has a

104 double-layer structure and fewer parameters. The horizontal structure is divided into river

105 channel units and slope units. The vertical structure below the surface is divided into a

106   shallow karst aquifer and a deep karst aquifer system. Only a small amount of

107   hydrogeological data is needed for modeling in karst basins.

108   To ensure that the QMG model work well in karst flood simulation and prediction in the

109   case of relatively simple structure and parameters. We carefully designed the algorithms of

110   runoff generation and confluence in the model. And to verify its applicability of QMG model

111   in flood simulation in karst basins, we selected the Qingmuguan karst trough valley in

112   Chongqing, China, as the study area for a flood simulation and uncertainty analysis. In

113   particular, the sensitivity of model parameters was analyzed.

114   **2. Study Area and Data**

115   2.1. Landform and topography

116   The Qingmuguan karst trough valley is located in the southeastern part of the Sichuan

117   Basin, China, at the junction of the Beibei and Shapingba districts in Chongqing, with

118   coordinates of 29°40′N ~ 29°47′N, 106°17′E ~ 106°20′E. The basin covers an area of 13.4

119   km² and is part of the southern extension of the anticline at Wintang Gorge in the Jinyun

120   Mountains, with the anticlinal axis of Qingmuguan located in a parallel valley in eastern

121   Sichuan (Yang et al., 2008). The surface of the anticline is heavily fragmented, and faults

122   are extremely well-developed with large areas of Triassic carbonate rocks exposed. Under

123   the long-term erosion of karst water, a typical karst landform pattern of "three mountains

124   and two troughs" has formed (Liu et al., 2009). Such karst trough landform provides

125   convenient conditions for flood propagation, and the karst landform development is

126   extremely common in the karst region of southwest China, especially in the karst region of

127   Chongqing. Similar regions include the karst trough valley of the Zhongliang Mountains and

128   the Laolongdong karst basin in Nanshan, Chongqing.

129   The basin is oriented north-north-east and south-south-west in a narrow band of slightly

130   curved arcs and is about 12 km long from north to south. The direction of the mountains in

131   the region is basically the same as the direction of the tectonic line. The difference in

132   relative elevation is between 200–300 m. Fig.1 is a map showing an overview of the

133   Qingmuguan karst basin.

134   Figure 1 The Qingmuguan karst basin.

135   2.2. Hydrogeological conditions

136   The Qingmuguan basin is located within the subtropical humid monsoon climate zone,

137   with an average temperature of 16.5℃ and a average precipitation of 1250 mm that is

138   mainly concentrated in May-September. An underground river system has developed in the

139   karst trough valley, with a length of 7.4 km, the water supply of underground river mainly

140   comes from rainfall recharge (Zhang, 2012). Most of the precipitation is collected along the

141   hill slope into the karst depressions at the bottom of the trough valley, where it is recharged

142   to the underground river through the dispersed infiltration of surface karst fissures and

143   concentrated injection from sinkholes (Fig. 1a). An upstream surface river collects in a

144   gentle valley and enters the underground river through the Yankou sinkhole (elevation 524

145   m). Surface water in the middle and lower reaches of the river system mainly enters the

146   underground river system through catenuliform sinkholes or fissures.

147   The stratigraphic and lithologic characteristics of the basin are largely dominated by

148   carbonate rocks of the Lower Triassic Jialingjiang Group (T_{1j}) and Middle Triassic Leikou

149   Slope Group (T_{2l}) on both sides of the slope, with some quartz sandstone and mudstone

150   outcrops of the Upper Triassic Xujiahe Group (T_{3xj}) (Zhang, 2012). The topography of the

151   basin presents a general anticline (Fig. 1b), where carbonate rocks on the surface are

152   corroded and fragmented, with a large permeability coefficient. Compared with the core of

153   the anticline, the rocks of the two wings of the anticline are less eroded and form a good

154   waterproof layer.

155   To investigate the karst conduits distribution in the underground river system, we

156   conducted a tracer test in the study area. The tracer was placed into the Yankou sinkhole and

157   recovered in the Jiangjia spring (Fig. 1a,c). According to the tracer test results (Gou et al.,

158   2010), the karst water-bearing medium in the aquifer was anisotropic, whereas the soluble

159   carbonate rocks were extremely permeable. The karst conduits in the underground river

160   were extremely well-developed, and there was a large single-channel underground river. The

161   response time of the underground river to rainfall was very fast, with the peak flow observed

162   at the outlet of Jiangjia spring 6–8 hours after rainfall. The flood peak rose quickly and the

163   duration of the peak flow was short. The underground river system in the study area is

164   dominated by large karst conduits, which is not conducive to water storage in water-bearing

165   media, but is very conducive to the propagation of floods.

166   2.3. Data

167   To build the QMG model to simulate the karst flood events, the necessary modelling

168   baseline data had to be collected, including: 1) high-resolution DEM data and

169   hydrogeological data (e.g., the thickness of the epikarst zone, rainfall infiltration coefficient

170   on different karst landforms, and permeability coefficient of rock); 2) land-use and soil type

171   data; and 3) rainfall data in the basin and water flow data of the underground river. The

172   DEM data was downloaded from a free database ~~on the public Internet~~, with an initial spatial

173   resolution of 30 × 30 m. The spatial resolution of landuse and soil types were 1000 × 1000

174   m, and they were also downloaded from the Internet. After considering the applicability of

175   modelling and computational strength, as well as the size of the basin in the study area (13.4

176   km^2), the spatial resolution of the three types of data was resampled uniformly in the QMG

177   model and downscaled to 15 × 15 m based on a spatial discrete method by Berry et, (2010).

178   The hydrogeological data necessary for modelling was obtained in three simple ways. 1)

179   A basin survey was conducted to obtain the thickness of the epikarst zone, which was

180   achieved by observing the rock formations on hillsides following cutting for road

181   construction. Information was collected regarding the location, general shape, and size of

182   karst depressions and sinkholes, which had a significant impact on compiling the DEM data

183   and determining the convergence process of surface runoff. 2) Empirical equations

184   developed for similar basins were used to obtain the rainfall infiltration coefficient for

185   different karst landforms and the permeability coefficient of rock. For example, the rock

186   permeability coefficient was calculated based on an empirical equation from a pumping test

187   in a coal mine in the study area (Li et al., 2019). 3) A tracer experiment was conducted in the

188 study area (Gou et al., 2010) to obtain information on the underground river direction and

189 flow velocity.

190   Rainfall and flood data are important model inputs, and represent the driving factors

191 that allow hydrological models to operate. In the study area, rainfall data was acquired by

192 two rain gauges located in the basin (Fig. 1a). Point rainfall was then spatially interpolated

193 into basin-level rainfall (for such a small basin area rainfall results obtained from two rain

194 gauges was considered representative). There were 18 karst flood events in the period of 14

195 April 2017 to 10 June 2019. We built a rectangular open channel at the underground river

196 outlet and set up a river gauge on it (Fig. 1a) to record the water level and flow data every 15

197 minutes.

198 **3. Methodology**

199 **3.1. Hydrological model**

200   The hydrological model developed in this study was named the QMG model after the

201 basin for which it was developed and to which it was first applied, i.e., the Qingmuguan

202 basin. The QMG model proposed in this study has a two-layer structure, including a surface

203 part and an underground part, with the former mainly performing the calculation of runoff

204 generation and the confluence of the surface river, while the latter performs the confluence

205 calculation of the underground river system.

206   The structure of the QMG model is divided into a two-layer structure, both horizontally

207 and vertically. The horizontal structure of the model is divided into river channel units and

208 slope units. The vertical structure below the surface is divided into a shallow karst aquifer

209 (including soil layers, karst fissures, and conduit systems in the epikarst zone) and a deep

210 karst aquifer system (rock stratum and underground river system). This relatively simple

211 model structure makes it need only a small amount of hydrogeological data when modeling

212 in karst regions. Fig. 2 shows a flowchart of the modeling and calculation procedures

213 required for the QMG model.

214   Figure 2 Modeling flow chart of QMG (Qingmuguan) model.

215   To accurately describe the runoff generation and confluence on a grid scale, these karst

216   sub-basins are further divided into a lot of karst hydrological response units (KHRUs). The

217   specific steps involved in the division were adopted by referring to studies of hydrological

218   response units (HRUs) in TOPMODEL by Pan (2014). As the smallest basin computing

219   units, the KHRUs can effectively ignore the spatial differences of karst development within

220   the units and reduce the uncertainty in the classification of model units. Fig. 3 shows the

221   spatial structure of the KHRUs.

222   Figure 3 Spatial structure of the KHRUs (Li et al.,2021).

223   The modeling and operation of the QMG model consists of three main stages: 1) spatial

224   interpolation, and the retention of rainfall and evaporation calculations; 2) runoff generation

225   and confluence calculation for the surface river; and 3) confluence calculation for the

226   underground runoff, including the confluence in the shallow karst aquifer and the

227   underground river system.

3.1.1. Rainfall and evaporation Calculation

229   In the QMG model, the spatial interpolation of rainfall is accomplished by a kriging

230   method using the ArcGIS 10.2 software. The Tyson polygon method may be a simpler

231   method for rainfall interpolation if the number of rainfall gauges in the basin is sufficient.

232   The point rainfall observed by the two rainfall gauges in the basin (Figure 1a) was spatially

233   interpolated into areal rainfall for the entire basin.

234   Basin evapotranspiration in the KHRUs was mainly vegetal, soil evaporation, and water

235   surface evaporation. They were calculated using the following equations (modified from Li

236   et al., 2020):

237
$$
\begin{cases}
E_v = V^{t+\Delta t} - V^t - P_v \\
E_s = \lambda E_p, \text{if } F = F_c \\
E_s = \lambda E_p \dfrac{F}{F_c}, \text{if } F < F_{sat} \\
E_w = \Delta e \cdot \left[1.12 + 0.62 \left(\Delta T \right)^{0.9} \right] \cdot \left[0.084 + 0.24 \left(1 - \gamma^2 \right)^{1/2} \right] \cdot \left[0.348 + 0.5 \omega^{1.8 \text{-} 1.137 \omega^{0.05}} \right]
\end{cases}
\tag{1}
$$

238   Here, E_v [mm] is the vegetal discharge, $V^{t+\Delta t} - V^t$ [mm] is the rainfall variation

239   by vegetation interception, P_v [mm] is the vegetation interception of rainfall, and E_s

240   [mm] is the actual soil evaporation. The term λ is the evaporation coefficient. The term

241   E_p [mm] is the evaporation capability, which can be measured experimentally or

242   estimated by the water surface evaporation equation E_w. The term F [mm] is the actual

243   soil moisture, F_{sat} [mm] is saturation moisture content, F_c [mm] is field capacity, E_w

244   [mm/d] is evaporation of water surface, and $\Delta e = e_0 - e_{150}$ [hPa] is the draught head

245   between the saturation vapor pressure of the water surface and the air vapor pressure

246   150 m above the water surface (150 m above the water surface was selected here

247   because the altitude for temperature and humidity observations in the southwestern

248   karst regions of China is usually set at 150–200 m). The term $\Delta T = t_0 - T_{150}$ [°C] is the

249   temperature difference between the water surface and the temperature 150 m above the

250   water surface, γ is the relative humidity 150 m above the water surface, and ω [m/s]

251   is the wind speed 150 m above the water surface.

252   **3.1.2. Runoff Generation**

253   In the QMG model, the surface runoff generation in river channel units means the

254   rainfall in the river system after deducting evaporation losses. This portion of the runoff will

255   participate in the confluence process directly through the river system, rather than

256   undergoing infiltration. In contrast, the process of runoff generation in slope units is more

257   complex, and its classification is related to the developmental characteristics of surface karst

258   in the basin, rainfall intensity, and soil moisture. For example, when the soil moisture

259   content is already saturated, there is the potential for excess infiltration surface runoff in

260   exposed karst slope units. The surface runoff generation of the KHRUs in the river channel

261   units and slope units can be described by the following equations (modified from Chen,

262   2009, 2018; Li et al., 2020):

263
$$\begin{cases} P_r(t) = \left[P_i(t) - E_p \right] \dfrac{L \cdot W_{max}}{A} \\ R_{si} = (P_i - f_i), P_i \geq f_{max} \\ R_{si} = 0, P_i < f_{max} \\ f_{max} = \alpha (F_c - F)^\beta + F_s \end{cases} \tag{2}$$

264   Here, $P_r(t)$ [mm] is the net rainfall (deducting evaporation losses) in the river channel

265   units at time t, hours; $P_i(t)$ [mm] is the rainfall in the river channel units, L [m] is the length

10

266   of the river channel, W_{max} [m] is the maximum width of the river channel selected, and A

267   [m^2] is the cross-sectional area of the river channel. R_{si} is termed excess infiltration runoff in

268   the QMG model, [mm]; when the vadose zone is short of water and has not been filled. The

269   infiltration capacity f_{max} is different in different karst landform units, α, β are Holtan model's

270   parameters; and F_s [mm] is the stable depth of soil water infiltration.

271   In the KHRUs (Fig. 3), underground runoff is generated primarily from the infiltration

272   of rainwater and direct confluence recharge from sinkholes or skylights. In the QMG model,

273   the underground runoff is calculated by the following equations (modified from Chen,

274   2018):

275
$$\begin{cases} R_g = R_0 \exp(-pt^m) \\ R_e = v_e \cdot I_w \cdot z \end{cases} \tag{3}$$

276   where

277
$$\begin{cases} \dfrac{\partial R_e}{\partial x} + I_w \cdot z \cdot \dfrac{\partial F}{\partial t} = R_r - R_{epi} \\ v_e = K \cdot \tan(\alpha), \quad F > F_c \\ v_e = 0, \quad F \le F_c \end{cases} \tag{4}$$

278   Here, R_g [mm] is the underground runoff depth (this part of the underground runoff is

279   mainly from the direct confluence supply of the karst sinkholes or skylights in the study

280   area), R_0 [mm] is the average depth of the underground runoff, p and m are attenuation

281   coefficients calculated by conducting a tracer test in the study area, R_e [L/s] is the

282   underground runoff generated from rainfall infiltration in the epikarst zone, I_w [mm] is the

283   width of the underground runoff on the KHRUs, z [mm] is the thickness of the epikarst zone,

284   R_r [mm^2/s] is the runoff recharge on the KHRUs during period t, R_{epi} [mm^2/s] is the water

285   infiltration from rainfall, v_e [mm/s] is the flow velocity of the underground runoff, K

286   [mm/s] is the current permeability coefficient, and α is the hydraulic gradient of the

287   underground runoff. If the current soil moisture is less than the field capacity, i.e., $F \le F_c$,

288   then the vadose zone is not yet full, there will be no underground runoff generation, and

289   rainfall infiltration at this time will continue to compensate for the lack of water in the

290   vadose zone until it is full and before runoff is generated.

291   **3.1.3. Channel Routing and Confluence**

292   In the QMG model, the calculation of runoff confluence on the KHRUs includes the

293   confluence of surface river channel and underground runoff. There are already many mature

294   and classical algorithms available for calculating the runoff confluence in river channel units

295   and slope units, such as the Saint-Venant equations and Muskingum convergence model. In

296   this study, the Saint-Venant equations were adopted to describe the confluence in the surface

297   river and hill slope units, for which a wave movement equation was adopted to calculate

298   confluence in slope units (Chen, 2009):

299
$$\begin{cases} \dfrac{\partial Q}{\partial x} + L\dfrac{\partial h}{\partial t} = q \\ S_f - S_0 = 0 \end{cases} \tag{5}$$

300   where

301
$$Q = vhL = \frac{L}{n} h^{\frac{5}{3}} S_0^{\frac{1}{2}}. \tag{6}$$

302   Here, we customized two variables a and b:

303
$$\begin{cases} a = (\dfrac{n}{L} S_0^{-\frac{1}{2}})^{\frac{3}{5}} \\ b = \dfrac{3}{5} \end{cases} \tag{7}$$

304   Equation (7) was substituted into equation (5) and discretized by a finite difference

305   method, giving

306
$$\begin{cases} \dfrac{\partial Q}{\partial x} + abQ^{(b-1)} \dfrac{\partial Q}{\partial t} - q = 0 \\ \dfrac{\Delta t}{\Delta x} Q_{i+1}^{t+1} + a(Q_{i+1}^{t+1})^b = \dfrac{\Delta t}{\Delta x} Q_i^{t+1} + a(Q_{i+1}^t)^b + q_{i+1}^{t+1}\Delta t \end{cases} \tag{8}$$

307   The Newton–Raphson method was used for the iterative calculation using equation (8):

308
$$\left[Q_{i+1}^{t+1}\right]^{k+1} = \left[Q_{i+1}^{t+1}\right]^{k} - \frac{\frac{\Delta t}{\Delta x}\left[Q_{i+1}^{t+1}\right]^{k} + a\left(\left[Q_{i+1}^{t+1}\right]^{k}\right)^{b} - \frac{\Delta t}{\Delta x}Q_{i}^{t+1} - a(Q_{i+1}^{t})^{b} - q_{i+1}^{t+1}\Delta t}{\frac{\Delta t}{\Delta x} + ab\left(\left[Q_{i+1}^{t+1}\right]^{k}\right)^{b-1}}, \quad (9)$$

309   where Q [L/s] is the confluence of water flow in slope units, L [dm] is its runoff width,

310   h [dm] is the runoff depth, and q [dm²/s] is the lateral inflow on the KHRUs. Here, the

311   friction slope S_f equals the hill slope S_0, and the inertia term and the pressure term in the

312   motion equation of the Saint-Venant equations were ignored. The term v [dm/s] is the flow

313   velocity of surface runoff in the slope units as calculated by the Manning equation, n is the

314   roughness coefficient of the slope units, Q_i^{t+1} [L/s] is the slope inflow in the KHRU at time

315   t+1, and Q_{i+1}^{t+1} [L/s] is the slope discharge in the upper adjacent KHRU at time t+1.

316   Similarly, the surface river channel confluence was described based on Saint-Venant

317   equation, where a diffusion wave movement equation was adopted, means the inertia term in

318   the motion equation was ignored:

319
$$\begin{cases} \dfrac{\partial Q}{\partial x} + \dfrac{\partial A}{\partial t} = q \\ S_f = S_0 - \dfrac{\partial h}{\partial x} \end{cases} \quad (10)$$

320   A finite difference method and the Newton–Raphson method were used for the iterative

321   calculation of the above equation:

322
$$\begin{cases} \left[Q_{i+1}^{t+1}\right]^{k+1} = \left[Q_{i+1}^{t+1}\right]^{k} - \dfrac{\frac{\Delta t}{\Delta x}\left[Q_{i+1}^{t+1}\right]^{k} + c\left(\left[Q_{i+1}^{t+1}\right]^{k}\right)^{b} - \frac{\Delta t}{\Delta x}Q_{i}^{t+1} - c(Q_{i+1}^{t})^{b} - q_{i+1}^{t+1}\Delta t}{\frac{\Delta t}{\Delta x} + cb\left(\left[Q_{i+1}^{t+1}\right]^{k}\right)^{b-1}} \\ c = (\dfrac{1}{3600}n\chi^{\frac{2}{3}}S_f^{-\frac{1}{2}})^{\frac{3}{5}} \end{cases}$$

323
(11)

324   where Q [L/s] is the water flow in surface river channel units, A [dm²] is the discharge

325   section area, c is a custom intermediate variable, and χ [dm] is the wetted perimeter of the

326   discharge section area.

327   The underground runoff in the model includes the confluence of epikarst zone and

328   underground river. In the epikarst zone, the karst water-bearing media are highly

329   heterogeneous. For example, the crisscrossed karst fissure systems and conduit systems

330   consisted of large corrosion fractures. When rainfall infiltrates into the epikarst zone, water

331   moves slowly through the small karst fissure systems, while it flows rapidly in larger

332   conduits. The key to determining the confluence velocity lies in the width of karst fractures.

333   In the KHRUs (Fig. 3), the 10-cm width of the fracture was used as a threshold value

334   (Atkinson, 1977), meaning that if the fracture width exceeded 10 cm, then the water

335   movement into it was defined as rapid flow; otherwise, it was defined as slow flow. The

336   confluence in the epikarst zone was calculated by the following equation (modified from

337   Beven and Binley, 2006):

338
$$Q(t)_{ijk} = b_{ijk} \cdot \frac{\Delta h}{\Delta l} R_i C_j \cdot T(t)_{\text{slow/rapid}} \qquad (12)$$

339   where

340
$$\begin{cases} T(t)_{\text{slow}} = nr \dfrac{\rho g R_i C_j L_k}{12v} \\[2mm] T(t)_{\text{rapid}} = \dfrac{K_{ij}\left(e^{-f_{ij}h_{ij}} - e^{-f_{ij}z_{ij}}\right)}{f_{ij}} \end{cases} \qquad (13)$$

341   Here, $Q(t)_{ijk}$ [L/s] is the flow confluence in the epikarst zone at time t, b_{ijk} [dm] is

342   the runoff width, $\dfrac{\Delta h}{\Delta l}$ is the dimensionless hydraulic gradient, $T(t)_{\text{slow/rapid}}$ is the

343   dimensionless hydraulic conductivity, ρ [g/L] is the density of the water flow, g [m/s^2] is

344   gravitational acceleration, n is the valid computational units, $R_i C_j L_k$ [L] is the volume of

345   the ijk-th KHRU, v is kinematic viscosity coefficient, f_{ij} is the attenuation coefficient in

346   the epikarst zone, h_{ij} [dm] is the depth of shallow groundwater, and z_{ij} [dm] is thickness of

347   epikarst zone.

348   The distinction between rapid and slow flows in the epikarst zone is not absolute. The

349   10-cm width of a karst fracture as the dividing threshold also has some subjectivity. In fact,

350   there is usually water exchange between the rapid and slow flows at the junction of large and

351   small fissures in karst aquifers. In the QMG model, this water exchange can be described

352   with this equation (modified form Li et al., 2021):

$$
\begin{cases}
Q = \alpha_{i,j,k} \left(h_n - h_{i,j,k} \right) \\
\alpha_{i,j,k} = \sum_{ip=1}^{np} \dfrac{\left(K_w \right)_{i,j,k} \pi d_{ip} \dfrac{1}{2} \left(\Delta l_{ip} \tau_{ip} \right)}{r_{ip}}
\end{cases}
\tag{14}
$$

354   Here, $\alpha_{i,j,k}$ [dm²/s] is the water exchange coefficient in the ijk-th KHRU,

355    $\left(h_n - h_{i,j,k} \right)$ [dm] is the water head difference between the rapid and slow flows at the

356   junction of large and small fissures in KHRUs, np is the number of fissure systems

357   connected to the adjacent conduit systems, $\left(K_w \right)_{i,j,k}$ [dm/s] is the permeability coefficient

358   at the junction of a fissure and conduit, d_{ip} and r_{ip} [dm] are the conduit diameter and

359   radius, respectively, Δl_{ip} [dm] is the length of the connection between conduits i and p, and

360   τ_{ip} is the conduit curvature. Some of the parameters in this equation, such as $\left(K_w \right)_{i,j,k}$

361   and $\left(h_n - h_{i,j,k} \right)$, were obtained by conducting an infiltration test in the study area.

362   The confluence of the underground river system plays an important role for the

363   confluence at the basin outlet. To facilitate the calculation of confluence in the QMG model,

364   the underground river systems can be generalized into large multiple conduit systems.

365   During floods, these conduit systems are mostly under pressure. Whether the water flow is

366   laminar or turbulent depends on the flow regime at that time. The water flow into these

367   conduits is calculated by the Hagen–Poiseuille equation and the Darcy–Weisbach equation

368   (Shoemaker et al., 2008):

$$
\begin{cases}
Q_{\text{laminar}} = -A \dfrac{g d^2 \partial h}{32 \nu \partial x} = -A \dfrac{\rho g d^2 \Delta h}{32 \mu \tau \Delta l} \\[2mm]
Q_{\text{turbulent}} = -2A \sqrt{\dfrac{2 g d \left| \Delta h \right|}{\Delta l \tau}} \log \left(\dfrac{H_c}{3.71 d} + \dfrac{2.51 \nu}{d \sqrt{\dfrac{2 g d^3 \left| \Delta h \right|}{\Delta l \tau}}} \right) \dfrac{\Delta h}{\left| \Delta h \right|}
\end{cases}
\tag{15}
$$

370   Here, Q_{laminar} [L/s] is the water flow of the laminar flow in the conduit systems, A

371   [dm^2] is the conduit cross-sectional area, d [dm] is the conduit diameter, ρ [kg/dm^3] is the

372   density of the underground river, $\nu = \mu / \rho$ is the coefficient of kinematic viscosity,

373    $\Delta h / \tau \Delta l$ is the hydraulic slope of the conduits, τ is the dimensionless conduit curvature,

374    $Q_{turbulent}$ [L/s] is the turbulent flow in the conduit systems, and H_c [dm] is the average

375   conduit wall height.

3.2. Parameter Optimization

377   In total, the QMG model has 12 parameters, of which flow direction and slope are

378   topographic parameters that can be determined from the DEM without parametric

379   optimization, while the remaining 10 parameters require calibration. Other distributed

380   hydrological models with multiple structures usually have many parameters. For example,

381   the Karst-Liuxihe model (Li et al., 2021) has 15 parameters that need to be calibrated. In the

382   QMG model, each parameter is normalized as

$$x_i = x^*_i / x_{i0}, \qquad (16)$$

384   where x_i is the dimensionless parameter value i after it is normalized, x^*_i is the

385   parameter value i with an actual physical property, and x_{i0} is the initial or final value of x_i.

386   Through the processing of equation (16), the value range of the model parameters is limited to

387   a hypercube $K_n = (X \mid 0 \le x_i \le 1, \ i = 1, 2, ..., n)$, which is a dimensionless value. Such a

388   normalized treatment can ignore the influence of the spatiotemporal variation of the

389   underlying surface attributes on the parameters and at the same time simplify the parameter

390   classification and parameter number of the model to a certain extent. Accordingly, the model

391   parameters can be further divided into rainfall-evaporation parameters, epikarst-zone

392   parameters, and underground-river parameters. Table 1 lists the parameters of the QMG

393   model.

Table 1 Parameters of QMG model.

395   Because the QMG model has relatively few parameters, it is possible to calibrate

396   them manually, which has the advantage that the operation is easy to implement and does

397   not require a special program for parameter optimization. However, the disadvantage is that

398 it is subjective, which can lead to great uncertainty in the manual parameter calibration

399 process. To compare the effects of parameter optimization on model performance, this study

400 used both a manual calibration of parameters and the improved chaotic particle swarm

401 algorithm (IPSO) for the automatic calibration of model parameters, and compared the

402 effects of both on flood simulation.

403   In general, the structure and parameters of a standard particle swarm algorithm

404 (PSO) are simple, with the initial parameter values obtained at random. For parameter

405 optimization in high-dimensional, multi-peak hydrological models, the standard PSO is

406 easily limited to a local convergence and cannot achieve the optimal effect, while the late

407 evolution of the algorithm may also cause problems, such as precocity and stagnant

408 evolution, due to the "inert" aggregation of particles, which seriously affects the efficiency

409 of parameter selection. It is necessary to overcome the above problems and make the

410 algorithm converge to the global optimal solution with a high probability. In parameter

411 optimization for the QMG model, we improved the standard PSO algorithm by adding chaos

412 theory, and developed the IPSO, where 10 cycles of chaotic disturbances were added to

413 improve the activity of the particles. The inverse mapping equation of the chaotic variable is

414 as follows:

415
$$\begin{cases} X_{ij} = X_{\min} + (X_{\max} - X_{\min}) * Z_{ij} \\ Z_{ij}^{'} = (1-\alpha)Z^{*} + \alpha Z_{ij} \end{cases} \tag{17}$$

416   where X_{ij} is the optimization variable for the model parameters, $(X_{\max} - X_{\min})$ is the

417 difference between its maximum and its minimum, Z_{ij} is the variable before the disturbance is

418 added, and $Z_{ij}^{'}$ represents the chaotic variables after a disturbance is added, α is a variable

419 determined by the adaptive algorithm, $0 \leq \alpha \leq 1$, and Z^{*} is the chaotic variable formed when

420 the optimal particle maps to the interval [0,1]. In parameter optimization, the flowchart of the

421 IPSO is shown in Fig. 4.

422   Figure 4 Algorithm flow chart of the IPSO.

3.3. Uncertainty Analysis

423

424   As a type of mathematical and physical model, a hydrological model has some

425   uncertainty in flood simulation and forecasting because of the errors in system structure and

426   the algorithm (Krzysztofowicz and Kelly, 2000). A multi-parametric sensitivity analysis

427   method (Choi et al., 1999; Li et al., 2020) was used to analyze the sensitivity of the

428   parameters in the QMG model. Parameter sensitivity analysis steps are as follows.

429   1) Selection of appropriate objective function

430   The Nash–Sutcliffe coefficient is widely used as the objective function to evaluate the

431   performance of hydrological models (Li et al., 2020, 2021). It was therefore used to assess

432   the QMG model. Because the most important factor in flood forecasting is the peak

433   discharge, it is used in the Nash coefficient equation:

$$NSC = 1 - \frac{\sum_{i=1}^{n}\left(Q_i - Q_i^{'}\right)^2}{\sum_{i=1}^{n}\left(Q_i - \overline{Q}\right)^2}, \qquad (18)$$

435   where NSC is Nash–Sutcliffe coefficient values, Q_i [L/s] is the observed flow discharges, Q_i'

436   [L/s] is the simulated discharge, $\overline{Q}$ [L/s] is the average value of the observed discharges,

437   and n [h] is the observation period.

438   2) Parameter sequence sampling

439   The Monte Carlo sampling method was applied to sample 8,000 groups of parameter

440   sequences. The parametric sensitivity of the QMG model was analyzed and evaluated by

441   comparing the differences between the a priori and a posteriori distributions of the

442   parameters.

443   3) Parameter sensitivity assessment

444   The a priori distribution maens its probability distribution of a model parameter, while

445   the a posteriori distribution can be calculated based on the simulation result of the

446   parametric optimization. If there is a significant difference between them, then the parameter

447   being tested has a high sensitivity, whereas if there is no obvious difference, then the

448   parameter is insensitive. The parametric priori distribution is calculated as follows:

18

449
$$\begin{cases} P_{i,j}(NSC_{i,j} \geq 0.85) = \dfrac{n}{N+1} \times 100 \\ \sigma_i = \sum_{j=1}^{n} \left(P_{i,j} - \overline{P_{i,j}} \right)^2 \end{cases}$$
(19)

450   where $P_{i,j}$ is the priori distribution'probability when $NSC_{i,j} \geq 0.85$. We used a

451   simulated Nash coefficient of 0.85 as the threshold value, and n was the number of

452   occurrences of a Nash coefficient greater than 0.85 in flood simulations. In each simulation,

453   only a certain parameter was changed, while the remaining parameters remained unchanged.

454   If the Nash coefficient of this simulation exceeded 0.85, then the flood simulation results

455   were considered acceptable. The term σ_i is the difference between the acceptable value

456   and its mean, which represents the parametric sensitivity ($0 < \sigma_i < 1$). The higher the σ_i

457   value, the more sensitive the parameter. N is the 8,000 parameter sequences, and $\overline{P_{i,j}}$ is the

458   average value of the a priori distribution.

459   **3.4. Model Setting**

460   Once the model was built, some of the initial conditions had to be set before running it

461   to simulate and forecast floods, such as basin division, the setting of initial soil moisture, and

462   the assumption of the initial parameter range. 1) In the study area, the entire Qingmuguan

463   karst basin was divided into 893 KHRUs, including 65 surface river units, 466 hill slope

464   units, and 362 underground river units. The division of these units formed the basis for

465   calculating the process of runoff generation and convergence. 2) The initial soil moisture

466   was set to 0–100% of the saturation moisture content in the basin, and the specific soil

467   moisture before each flood had to be determined by a trial calculation. 3) The waterhead

468   boundary conditions of the groundwater were determined by a tracer test in the basin, where

469   a perennial stable water level adjacent the groundwater-divide was used as the fixed

470   waterhead boundary. The base flow of the underground river was determined to be 35 L/s

471   from the perennial average dry season runoff. 4) The range of initial parameters and

472   convergence conditions were assumed before parameter optimization (Figure 4). 5)

473   Parameter optimization and flood simulation validated the performance of the QMG model

474   in karst basins.

475   **4. Results and Discussion**

476   **4.1. Parameter Sensitivity Results**

477   The number of parameters in a distributed hydrological model is generally large, and it

478   is important to perform a sensitivity analysis of each parameter to quantitatively assess the

479   impact of the different parameters on model performance. In the QMG model, each

480   parameter was divided into four categories according to its sensitivity: (i) highly sensitive,

481   (ii) sensitive, (iii) moderately sensitive, and (v) insensitive. In the calibration of model

482   parameters, insensitive ones do not need to be calibrated, which can greatly reduce the

483   amount of calculation and improve the efficiency of model operation.

484   The flow process in the calibration period (14 April to 10 May 2017) was adopted to

485   calculate the sensitivity of the model parameters, for which the calculation principle was

486   equation (19), and the parameter sensitivity results are calculated in Table 2.

487   Table 2 Parametric sensitivity results in QMG model.

488   In Table 2, the value of σ_i [equation (19)] represents a parameter's sensitivity, and the

489   higher the value, the more sensitive the parameter is. From the results in Table 2, it was

490   found that the rainfall infiltration coefficient, rock permeability coefficient, rock porosity,

491   and the related parameters of soil water content, such as the saturated water content, and

492   field capacity, were sensitive parameters. The order of parameter sensitivity was as follows:

493   infiltration coefficient > permeability coefficient > rock porosity > specific yield > saturated

494   water content > field capacity > flow direction > thickness > slope > Soil coefficient >

495   channel roughness > evaporation coefficient.

496   In the QMG model, parameters are classified as highly sensitive, sensitive, moderately

497   sensitive, and insensitive according to their influence on the flood simulation results. In

498   Table 4, we divided the sensitivity of model parameters into four levels based on the σ_i

499   value: 1) highly sensitive parameters, $0.8 < \sigma_i < 1$; 2) sensitive parameters, $0.65 < \sigma_i < 0.8$;

500 3) moderately sensitive parameters, $0.45 < \sigma_i < 0.65$; and 4) insensitive parameters,

501 $0 < \sigma_i < 0.45$. The highly sensitive parameters were the infiltration coefficient, permeability

502 coefficient, rock porosity, and specific yield. The sensitive parameters were the saturated

503 water content, field capacity, and thickness of the epikarst zone. The moderately sensitive

504 parameters were flow direction, slope, and soil coefficient. The insensitive parameters were

505 channel roughness and the evaporation coefficient.

506 **4.2. Parametric Optimization**

507 In total, the QMG model has 12 parameters, of which only eight need to be optimized,

508 which is relatively few for distributed models. The parameters of flow direction and slope as

509 well as the insensitive parameters of channel roughness and the evaporation coefficient need

510 not be calibrated, which can improve the convergence efficiency of the model parameter

511 optimization.

512 In the study area, 18 karst floods during the period of 14 April 2017 to 10 June 2019

513 were recorded at underground river outlet to validate the effects of the QMG model in karst

514 hydrological simulations. The calibration period was 14 April to 10 May 2017 at the

515 beginning of the flow process, with the remainder of the time being the validation period. In

516 the QMG model, the IPSO algorithm was used to optimize the model parameters. To show

517 the necessity of parameter optimization for the distributed hydrological model, the study

518 specifically compared the flood simulations obtained using the initial parameters of the

519 model (without parameter calibration) and the optimized parameters. Fig. 5 shows the

520 iteration process of parameter optimization for the QMG model.

521 Figure 5 Iteration process of parametric optimization.

522 Fig. 5 shows that almost all parameters fluctuated widely at the beginning of the

523 optimization, and then after about 15 iterations of the optimization calculation, most of the

524 linear fluctuations become significantly less volatile, which indicated that the algorithm

525 tended to converge (possibly only locally). When the number of iterations exceeded 25, all

526 parameters remained essentially unchanged, meaning that the algorithm had converged (at

527 this point there was global convergence). It took only 25 iterations to reach a definite

528   convergence of the parameter rates with this IPSO algorithm, which is extremely efficient in

529   terms of the parameter optimization of distributed hydrological models. In previous studies

530   of the parametric optimization for the Karst-Liuxihe model in similar basin areas, 50

531   automatic parameter optimization iterations were required to reach convergence (Li et al.,

532   2021), demonstrating the effectiveness of the IPSO algorithm.

533   To evaluate the effect of parameter optimization, the convergence efficiency of the

534   algorithm, and more importantly, the parameters after calibration were used to simulate

535   floods. Fig. 6 shows the flood simulation effects.

536   Figure 6 Flow simulation results of QMG model based on parameter optimization.

537   Fig. 6 shows that the flows simulated by parameter optimization were better than those

538   simulated by the initial model parameters. The simulated flow processes based on the initial

539   parameters were relatively small, with the simulated peak flows in particular being smaller

540   than the observed values, and there were large errors between the two values. In contrast, the

541   simulated flows produced by the QMG model after parameter optimization were very

542   similar to the observed values, which indicates that calibration of the model parameters is

543   necessary and that there was an improvement in parameter optimization through the use of

544   the IPSO algorithm in this study. In addition, it was found that the flow simulation effect

545   was better in the calibration periods than in the validation periods (Fig. 6).

546   To compare the results of the flow processes simulation with the initial model

547   parameters and the optimized parameters, six evaluation indices (Nash–Sutcliffe coefficient,

548   correlation coefficient, relative flow process error, flood peak error, water balance

549   coefficient, and peak time error) were applied in this study, and the results are presented in

550   Table 3.

551   Table 3 Flood simulation evaluation index through parametric optimization.

552   Table 3 shows that the evaluation indices of the flood simulations after parametric

553   optimization were better than those of the initial model parameters. The average values of

554   the initial parameters for these six indices 0.81, 0.74, 27%, 31%, 0.80, and 5 h, respectively.

555   For the optimized parameters, the average values were 0.90, 0.91, 16%, 14%, 0.94, and 3 h,

556   respectively. The flood simulation effects after parameter optimization clearly improved,

557   implying that parameter optimization for the QMG model is necessary, and the IPSO

558   algorithm for parameter optimization is an effective approach that can greatly improve the

559   convergence efficiency of parameter optimization, and also ensure that the model performs

560   well in flood simulations.

561   **4.3. Model Validation in Flood Simulations**

562   Following parameter optimization, we simulated the whole flow process (14 April 2017

563   to 10 June 2019) based on the optimized and initial parameters of the QMG model (Fig. 6),

564   which enabled a visual reflection of the model used in the simulation of a long series of flow

565   processes. To reflect the simulation effect of the model for different flood events, we divided

566   the whole flow process into 18 flood events, then used the initial parameters of the model

567   and the optimized parameters, respectively, to verify the model performance in flood

568   simulations. Fig. 7 and Table 4 show the flood simulation effects and their evaluation indices

569   using both the initial and the optimized parameters.

570   Figure 7 Flood simulation effects based on initial and optimized parameters.

571   Table 4 Flood simulation indices for model validation.

572   Fig. 7 shows that the flood simulation results using the initial parameters were smaller

573   than the observed values, and the model performance improved in flood simulations after

574   parameter optimization. The simulated flood processes were in good agreement with

575   observations, and were especially effective for simulating flood peak flows. From flood

576   simulation indices in Table 4, the average water balance coefficient based on the initial

577   parameters was 0.69, i.e., much less than 1, indicating that the simulated water in the model

578   was unbalanced. After parameter optimization, the average value was 0.92, indicating that

579   parameter optimization had a significant impact on the model water balance calculation.

580   Table 4 shows that the average values of the six indices (Nash–Sutcliffe coefficient,

581   correlation coefficient, relative flow process error, flood peak error, water balance

582   coefficient, and peak time error) for the initial parameters were 0.79, 0.74, 26%, 25%, 0.69,

583   and 5 h, respectively, while for the optimized parameters the average values were 0.92, 0.90,

584   10%, 11%, 0.92, and 2 h, respectively. All evaluation indices improved after parameter

585   optimization, with the average values of the Nash coefficient, correlation coefficient, and

586   water balance coefficient increasing by 0.13, 0.16, and 0.23, respectively. The average

587   values of the relative flow process error, flood peak error, and peak time error decreased by

588   15%, 14%, and 3 h, respectively. These reasonable flood simulation results confirmed that

589   parameter optimization by the IPSO algorithm was necessary and effective for the QMG

590   model.

591   Compared with the overall flow process simulation shown in Figure 6, each flood

592   process was better simulated by the QMG model (Fig. 7). This was because in the function

593   of the QMG model and its algorithm design, the main consideration was the calculation of

594   the flood process, but the correlation algorithm of the dry season runoff was not described

595   well enough. For example, equations (12)–(15) are the flood convergence algorithm. As a

596   result, the model is not good at simulating other flow processes, such as dry season runoff,

597   leading to a low accuracy in the overall flow process. The next phase of our research will

598   focus on refining the algorithm related to dry season runoff and improving the

599   comprehensive performance of the model.

600   **4.4. Uncertainty Analysis**

601   **4.4.1 Assessment and Reduction of Uncertainty**

602   In general, the uncertainty in model simulations are mainly derived from three aspects

603   of the model: 1) the uncertainty of the model input data, 2) the uncertainty of model

604   structure and the algorithm, and 3) the uncertainty of model parameters. In the practical

605   application of a hydrological model, these three uncertainties are usually interwoven, which

606   leads to the overall uncertainty of the final simulation results (Krzysztofowicz, 2014).

607   Therefore, this study focused on the input data, the model structure, and parameter

608   uncertainty to reduce the overall uncertainty of simulation results.

609   First, the input data (e.g., rainfall, flood event, and some hydrogeological data) were

610   validated and pre-processed through observations in this study, which substantially reduced

611   the uncertainty.

612   Second, we simplified the structure of the QMG model. The model was designed with

613   full consideration of the relationship between the amount of data required to build the model

614   and its performance for flood simulation and forecasting in karst regions, and the model's

615   entire framework was integrated through simple structures and easy-to-implement

616   algorithms, using the concept of distributed hydrological modeling. Conventionally, the

617   extent of uncertainty is increased with the growing complexity of the model structure. We

618   therefore ensured that the structure of the QMG model was simple when it was designed,

619   and the model was divided into surface and underground double layer structures. Such a

620   relatively simple structure made the uncertainty of the model structure reduced largely. In

621   contrast, the underground structure of our previous Karst-Liuxihe model (Li et al., 2021) has

622   five layers, which leads to great uncertainty.

623   Third, appropriate algorithms for runoff generation and confluence were selected. The

624   design function of different models is different, which leads to great differences in the

625   algorithms used. In the QMG model, most of the rainfall-runoff algorithms used have been

626   validated by the research results of others, and some of them were improved to suit karst

627   flood simulation and forecasting by the QMG model. For example, the algorithm of excess

628   infiltration runoff generation [equation (2)] was an improvement of the version used in the

629   Liuxihe model (Chen, 2009, 2018; Li et al., 2020).

630   Finally, the algorithm of parameter optimization was improved. Considering the

631   shortcomings of the standard PSO algorithm that tends to reach a local convergence, this

632   study developed the IPSO for parameter optimization by adding chaotic perturbation factors.

633   The flood simulation results after parameter optimization were much better than those of the

634   initial model parameters (Figs. 6 and 7 and Tables 2 and 3), which indicates that parameter

635   optimization is necessary for a distributed hydrological model and can reduce the

636   uncertainty of model parameters.

4.4.2 Parameter Sensitivity Analysis

638   From the results of parameter sensitivity in Table 2, it can be seen that the rainfall

639   infiltration coefficient in the QMG model was the most sensitive parameter. It was the key to

640   determining the generation of excess infiltration surface runoff and dividing surface runoff

641   from subsurface runoff. If the rainfall infiltration coefficient was greater than the infiltration

642   capacity, it would generate excess infiltration surface runoff on the exposed karst landforms;

643   otherwise, all rainfall would infiltrate to meet the water deficit in the vadose zone, and then

644   continue to seep down into the underground river system, eventually flowing out of the basin

645   through the underground river outlet. The confluence modes of surface runoff and

646   underground runoff were completely different, resulting in a large difference in the

647   simulated flow results. Therefore, the rainfall infiltration coefficient had the greatest impact

648   on the final flood simulation results.

649   Other highly sensitive parameters such as the rock permeability coefficient, rock

650   porosity, and specific yield were used as the basis for the division of slow flow in karst

651   fissures and rapid flow in conduits. The division of slow and rapid flows also had a great

652   impact on the discharge at the outlet of the basin. Slow flow plays an important role in water

653   storage in a karst aquifer and is very important for the replenishment of river base flow in

654   the dry season. Rapid flow in large conduit systems dominates of the flood runoff and is the

655   main component of the flood water volume in the flood season.

656   Parameters related to the soil water content, including the saturated water content, field

657   capacity, and thickness, were sensitive parameters and had a large influence on the flood

658   simulation results. This is because the soil moisture content prior to flooding affects how

659   flood flows rise and when peaks occur. If the soil is already very wet or even saturated

660   before the flooding, the flood will quickly rise to reach a peak, and the process line of the

661   flood peak flow will be sharp and thin. This type of flood process forms easily and can lead

662   to disaster-causing flood events. In contrast, if the soil in the basin is very dry before the

663   flooding, the rainfall will first meet the water shortage of the vadose zone, and after it is

664   replenished the rainfall will infiltrate into the underground river. The flood peak of the river

665   basin outlet is therefore delayed.

666   The moderately sensitive parameters were flow direction, slope, and the soil coefficient.

667   They had a specific influence on the flood simulation results, but the influence was not as

668   great as the highly sensitive and sensitive parameters. The insensitive parameters were

669 channel roughness and the evaporation coefficient. The amount of water lost by

670 evapotranspiration is very small in the total flood water, and it was therefore the least

671 sensitive parameter in the QMG model.

5. Conclusions

673 This study proposed a new distributed physically based hydrological model, i.e., the

674 QMG model, to simulate floods accurately in karst trough valley. The main conclusions of

675 this paper are as follows.

676 This QMG model has a high application potential in karst hydrology simulations. Other

677 distributed hydrological models usually have multiple structures, resulting in the need for a

678 large amount of data to build models in karst areas (Kraller et al., 2014). The QMG model

679 has only a double-layer structure, with a clear physical meaning, and a small amount of

680 basic data is needed to build the model in karst areas, such as some necessary

681 hydrogeological data. For example, the distribution and flow direction of underground rivers

682 is required, which can be inferred from a tracer test, leading to a low modeling cost. There

683 were fewer parameters in the QMG model than in other distributed hydrological models,

684 with only 10 parameters that needed to be calibrated.

685 The flood simulation after parameter optimization was much better than the simulation

686 using the initial model parameters. After parameter optimization, the average value of Nash

687 coefficient, correlation coefficient, and water balance coefficient increased by 0.13, 0.16,

688 and 0.23, respectively; while the average relative flow process error, flood peak error, and

689 peak time error decreased by 15%, 14%, and 3 h, respectively. Parameter optimization is

690 necessary for a distributed hydrological model, and the improvement of the IPSO algorithm

691 in this study was an effective way to achieve this.

692 In the QMG model, the rainfall infiltration coefficient, I_c, rock permeability coefficient,

693 K, rock porosity, R_p, and the parameters related to the soil water content were sensitive

694 parameters. The order of parameter sensitivity was: infiltration coefficient > permeability

695 coefficient > rock porosity > specific yield > saturated water content > field capacity > flow

696 direction > thickness > slope > soil coefficient > channel roughness > evaporation

697 coefficient.

698 This QMG model is suitable for karst trough valley basins, where the topography is

699 conducive to the spread of flood water. Whether this model is applicable to other karst areas

700 in non-trough valley regions still needs to be verified in the future studies. In addition, the

701 basin area is very small, where the hydrological similarity between different small basin

702 areas varies greatly (Kong and Rui, 2003). The size of the area to be modeled has a great

703 influence on the choice of model spatial resolution (Chen et al., 2017). Therefore, whether

704 the QMG model is suitable for flood forecasting in large karst basins needs to be

705 determined.

706 **Model development.**

707 This QMG model presented in this study uses the Visual Basic language programming. The
708 general framework of the model and the algorithm consist of three parts: the modeling
709 approach, the algorithm of rainfall-runoff generation and confluence, and the parameter
710 optimization algorithm. As a free and open source hydrological modeling program (QMG
711 model-V1.0), we provide all modeling packages, including model code, installation package,
712 simulation data package and user manual, free of charge. It is important to note that the
713 model we provide are for scientific research purposes only and should not be used for any
714 commercial purposes. Creative Commons Attribution 4.0 International.
715 Model installation program can be downloaded from ZENODO, cite as JI LI. (2021, June
716 16). QMG model-V1.0. Zenodo. http://doi.org/10.5281/zenodo.4964701, and
717 http://doi.org/10.5281/zenodo.4964697 (registration required). User manual can be
718 downloaded from http://doi.org/10.5281/zenodo.4964754.

719 **Code availability.**

720 All code for the QMG model-V1.0 in this paper are available and free, the code can be
721 downloaded from ZENODO, Cite as JI LI. (2021, June 16). QMG model-V1.0 code
722 (Version v1.0). Zenodo. http://doi.org/10.5281/zenodo.4964709 (registration required).

723 **Data availability.**

724 All data used in this paper are available, findable, accessible, interoperable, and reusable.
725 The simulation data and modelling data package can be downloaded from
726 http://doi.org/10.5281/zenodo.4964727. The DEM was downloaded from the Shuttle Radar
727 Topography Mission database at http://srtm.csi.cgiar.org. The land use-type data were
728 downloaded from http://landcover.usgs.gov,   and the soil-type data were downloaded from
729 http://www.isric.org. These data were last accessed on 15 October 2020.

730 **Author contributions.** JIL was responsible for the calculations and writing of the whole

731   paper. DY and YJ helped conceive the structure of the model. ZF and JL provided significant

732   assistance in the English translation of the paper. MM provided flow data of the study area.

733   **Competing interests.**

734   The authors declare that they have no conflicts of interest.

735   **Acknowledgments.**

740 **References**

741 Abbott, M. B., Bathurst, J. C., Cunge, J. A., O'Connell, P. E., and Rasmussen, J.: An
742   Introduction to the European HydrologicSystem-System Hydrologue Europeen, 'SHE',
743   a: History and Philosophy of a Physically-based, Distributed Modelling System,J.
744   Hydrol., 87, 45–59, 1986a.

745 Abbott, M. B., Bathurst, J. C., Cunge, J. A., O'Connell, P. E., and Rasmussen, J.: An
746   Introduction to the European Hydrologic System-System Hydrologue Europeen, 'SHE',
747   b: Structure of a Physically based, distributed modeling System, J. Hydrol., 87,61–77,
748   1986b.

749 Ambroise, B., Beven, K., and Freer, J.: Toward a generalization of the TOPMODEL
750   concepts: Topographic indices of hydrologic similarity. Water Resources Research, 32,
751   2135-2145, 1996.

752 Atkinson, T.C.: Diffuse flow and conduit flow in limestone terrain in the Mendip Hills,
753   Somerset (Great Britain). Journal of Hydrology, 35, 93-110.
754   https://doi.org/10.1016/0022-1694(77)90079-8, 1977.

755 Berry, R.A., Saurel, R., and Lemetayer, O.: The discrete equation method (DEM) for fully
756   compressible, two-phase flows in ducts of spatially varying cross-section. Nuclear
757   Engineering & Design, 240(11), 3797-3818, 2010.

758 Beven, K., and Binley, A.: The future of distributed models: Model calibration and
759   uncertainty prediction. Hydrological Processes, 6, 279-298, 2006.

760 Birk, S., Geyer, T., Liedl, R., and Sauter, M.: Process-based interpretation of tracer tests in
761   carbonate aquifers. Ground Water, 43(3), 381-388, 2005.

762 Bittner, D., Parente, M.T., Mattis, S., Wohlmuth, B., and Chiogna, G.: Identifying relevant
763   hydrological and catchment properties in active subspaces: An inference study of a
764   lumped karst aquifer model. ADVANCES IN WATER RESOURCES,135,550-560.

765   doi: 10.1016/j.advwatres.2019.103472, 2020.

766   Blansett, K. L., and Hamlett, J. M.: Challenges of Stormwater Modeling for Urbanized Karst
767   Basins. Pittsburgh, Pennsylvania, an ASABE Meeting Presentation, Paper Number:
768   1009274. doi:10.13031/2013.29840, 2010.

769   Blansett, K. L.: Flow, water quality, and SWMM model analysis for five urban karst basins..
770   (Doctoral dissertation). The Pennsylvania State University,USA, 2011.

771   Chang, Y., and Liu, L.: A review of hydrological models in karst areas. Engineering
772   investigation, 43,37-44, 2015.

773   Chen, G.M., Jia, J.Y., and Han, Q.: Research on inertia weight reduction strategy of Particle
774   Swarm optimization algorithm. Journal of Xi'an Jiaotong University, 40(1),53-56, 2006.

775   Choi, J., Harvey, J. W., and Conklin, M. H.: Use of multi-parameter sensitivity analysis to
776   determine relative importance of factors influencing natural attenuation of mining
777   contaminants. the Toxic Substances Hydrology Program Meeting, Charleston,South
778   Carolina, 1999.

779   Chen, Y. B.: Liuxihe Model, China Science and Technology Press, Beijing, China, 2009.

780   Chen, Y., Li, J., and Xu, H.: Improving flood forecasting capability of physically based
781   distributed hydrological models by parameter optimization. Hydrol. Earth Syst. Sci. 20,
782   375-392. https://doi.org/10.5194/hess-20-375-2016, 2016.

783   Chen, Y., Li, J., Wang, H., Qin, J., and Dong, L.: Large watershed flood forecasting with
784   high-resolution distributed hydrological model. Hydrol. Earth Syst. Sci. 21, 735-749.
785   https://doi.org/10.5194/hess-21-735-2017, 2017.

786   Chen, Y.: Distributed Hydrological Models. Springer Berlin Heidelberg, Berlin, Germany.
787   https://doi.org/10.1007/978-3-642-40457-3_23-1, 2018.

788   Dewandel, B., Lachassagne, P., Bakalowicz, M., Weng, P., and Malki, A.A.: Evaluation of
789   aquifer thickness by analysing recession hydrographs. Application to the Oman
790   ophiolite hard-rock aquifer. Journal of Hydrology, 274,248-269, 2003.

791   Dubois, E., Doummar, J., Séverin Pistre, S., and Larocque, M.: Calibration of a lumped karst
792   system model and application to the Qachqouch karst spring (Lebanon) under climate

793   change   conditions.   Hydrol.   Earth   Syst.   Sci.,   24,   4275-4290.

794   https://doi.org/10.5194/hess-24-4275-2020, 2020.

795 Doummar, J., Sauter, M., and Geyer, T.: Simulation of flow processes in a large scale karst

796   system with an integrated catchment model (MIKE SHE) – identification of relevant

797   parameters influencing spring discharge. Journal of Hydrology, 426-427, 112-123,

798   2012.

799 Epting, J., Page, R.M., and Auckenthaler, A.: Process-based monitoring and modeling of

800   Karst springs–Linking intrinsic to specific vulnerability. Science of the Total

801   Environment, 625, 403-415, 2018.

802 Fleury, P., Plagnes, V., and Bakalowicz, M.: Modelling of the functioning of karst aquifers

803   with a reservoir model: Application to Fontaine de Vaucluse (South of France). Journal

804   of Hydrology, 345,38-49. http://dx.doi.org/10.1016/j.jhydrol.2007.07.014, 2007b.

805 Ford, D. C., and Williams, P.W.: Karst geomorphology and hydrology. Wiley, Chichester,

806   England, 2007.

807 Gang, L., Tong, F.G., and Bin,T.: A Finite Element Model for Simulating Surface Runoff and

808   Unsaturated Seepage Flow in the Shallow Subsurface. Hydrological Processes,

809   6,102-120. doi: 10.1002/hyp.13564, 2019.

810 Geyer, T., Birk, S., Liedl, R., and Sauter, M.: Quantification of temporal distribution of

811   recharge in karst systems from spring hydrographs. Journal of Hydrology, 348(30),

812   452-463, 2008.

813 Gou, P.F., Jiang, Y.J., Hu, Z.Y., Pu, J.B., and Yang, P.H.: A study of the variations in

814   hydrology and hydrochemistry under the condition of a storm in a typical karst

815   subterranean stream. HYDROGEOLOGY&ENGINEERING GEOLOGY,37(5),20-25,

816   2010.

817 Hartmann, A., and Baker, A.: Progress in the hydrologic simulation of time variant of karst

818   systems-Exemplified at a karst spring in Southern Spain. Advances in Water Resources,

819   54,149-160, 2013.

820 Hartmann, A., Goldscheider, N., Wagener, T., Lange, J., and Weiler, M.: Karst water
821   resources in a changing world: Review of hydrological modeling approaches. Reviews
822   of Geophysics 52: 218-242. doi: 10.1002/2013RG000443, 2014a.

823 Hartmann, A., and Baker, A.: Modelling karst vadose zone hydrology and its relevance for
824   paleoclimate reconstruction. Earth-Science Reviews, 172, 178-192, 2017.

825 Hartmann, A.: Experiences in calibrating and evaluating lumped karst hydrological models.
826   London: Geological Society, Special Publications, 2018.

827 Jukić, D., and Denić-Jukić, V.: Groundwater balance estimation in karst by using a
828   conceptual   rainfall–runoff   model.   Journal   of   Hydrology,   373,   302-315.
829   http://dx.doi.org/10.1016/j.jhydrol.2009.04.035, 2009.

830 Kong, F.Z., and Rui, X.F.: Hydrological similarity of catchments based on topography.
831   GEOGRAPHICAL RESEARCH, (06), 709-715, 2003.

832 Kovács, A., and Sauter, M.: Modelling karst hydrodynamics. In: Goldscheider N, Drew D
833   (eds) Methods in karst hydrogeology, IAH international contributions to hydrogeology;
834   26,264 p, 2007.

835 Kovács, A., and Perrochet, P.: A quantitative approach to spring hydrograph decomposition.
836   Journal of Hydrology, 352, 16-29. http://dx.doi.org/10.1016/j.jhydrol.2007.12.009,
837   2008.

838 Kurtulus, B., and Razack, M.: Evaluation of the ability of an artificial neural network model
839   to simulate the input-output responses of a large karstic aquifer: the la rochefoucauld
840   aquifer (charente, france). Hydrogeology Journal, 15(2), 241-254, 2007.

841 Krzysztofowicz, R., and Kelly, K.: Hydrologic uncertainty processor for probabilistic river
842   stage forecasting. Water Resources Research, 36(11),3265-3277, 2000.

843 Krzysztofowicz, R.: Probabilistic flood forecast：Exact and approximate predictive
844   distributions. Journal of Hydrology, 517(1), 643-651, 2014.

845 Kraller, G., Warscher, M., Strasser, U., Kunstmann, H., and Franz, H.: Distributed
846   hydrological modeling and model adaption in high alpine karst at regional scale

847   (berchtesgaden alps, germany). Springer International Publishing Switzerland.

848   https://doi.org/10.1007/978-3-319-06139-9_8, 2014.

849   Ladouche, B., Marechal, J. C., and Dorfliger, N.: Semi-distributed lumped model of a karst

850   system under active management. Journal of Hydrology, 509,215-230, 2014.

851   Li, J., Chen, Y., Wang, H., Qin, J., Li, J., and Chiao, S.: Extending flood forecasting lead

852   time in a large basin by coupling WRF QPF with a distributed hydrological model,

853   Hydrol. Earth Syst. Sci. 21, 1279–1294. https://doi.org/10.5194/hess-21-1279-2017,

854   2017.

855   Li, J., Yuan, D., Liu, J., Jiang, Y., Chen, Y., Hsu, K. L., and Sorooshian, S.: Predicting floods

856   in a large karst river basin by coupling PERSIANN-CCS QPEs with a physically based

857   distributed hydrological model. Hydrol. Earth Syst. Sci. 23, 1505-1532.

858   https://doi.org/10.5194/hess-23-1505-2019, 2019.

859   Li, J., Hong, A., Yuan, D., Jiang,Y., Deng,S., Cao,C., and Liu, J.: A new distributed

860   karst-tunnel hydrological model and tunnel hydrological effect simulations. Journal of

861   Hydrology, 593, 125639. https://doi.org/10.1016/j.jhydrol.2020.125639, 2020.

862   Li, J., Hong, A., Yuan, D., Jiang,Y., Zhang,Y., Deng,S., Cao,C., Liu, J., and Chen,Y.:

863   Elaborate Simulations and Forecasting of the Effects of Urbanization on Karst Flood

864   Events Using the Improved Karst-Liuxihe Model.CATENA,197,104990.

865   https://doi.org/10.1016/j.catena.2020.104990, 2021.

866   Liedl, R.., Sauter, M., Huckinghaus, D., Clemens, T., and Teutsch, G.: Simulation of the

867   development of karst aquifers using a coupled continuum pipe flow model. Water

868   Resources Research, 39, 50-57, 2003.

869   Liu, X., Jiang, Y.J., Ye, M.Y., Yang, P.H., Hu, Z.Y., and Li, Y.Q.: Study on hydrologic regime

870   of underground river in typical karst valley- A case study on the Qingmuguan

871   subterranean stream in Chongqing. CARSOLOGICA SINICA, 28(2),149-154, 2009.

872   Lu, D. B., Shi, Z. T., Gu, S. X., and Zeng, J. J.: Application of Hydrological Model in the

873   Karst Area. Water-saving irrigation.11, 31-34. doi:1007-4929(2013)11-031-04, 2013.

874 Mario, T.P., Daniel, B., Steven, A. M., Gabriele, C., and Barbara, W.: Bayesian calibration

875 and sensitivity analysis for a karst aquifer model using active subspaces. Water

876 Resources Research, 55,342-356. doi: 10.1029/2019WR024739, 2019.

877 Meng, H.H., and Wang, N.C.: Advances in the study of hydrological models in karst basin.

878 Progress in Geography, 29,1311-1318, 2010.

879 Pan, H.Y.: Hydrological model and application in karst watersheds. China University of

880 Geosciences. Doctoral Dissertation, Wuhan, China, 2014.

881 Peterson, E.W., and Wicks, C. M.: Assessing the importance of conduit geometry and

882 physical parameters in karst systems using the storm water management model

883 (SWMM).Journal of Hydrology, 329, 1-2, 294-305, 2006.

884 Peterson, J.R., and Hamlett, J.M.: Hydrologic calibration of the SWAT model in a basin

885 containing fragipan soils. JAWRA Journal of the American Water Resources

886 Association. doi: 10.1111/j.1752-1688.1998. tb00952.x, 1998.

887 Petrie, R., Denvil, S., Ames, S.,et al.: Coordinating an operational data distribution network

888 for CMIP6 data, Geosci. Model Dev., 14, 629–644,

889 https://doi.org/10.5194/gmd-14-629-2021, 2021.

890 Qin, J.G., and Jiang, Y.P.: A review of numerical simulation methods for CFP pipeline flow.

891 Groundwater. 3, 98-100, 2014.

892 Reimann, T., Melissa, E., and Hill.: Modflow-cfp: a new conduit flow process for

893 modflow–2005. Ground Water,47(3),321-325. doi:10.1111/j.1745-6584.2009.00561.x,

894 2009.

895 Ren, Q.W.: Water Quantity Evaluation Methodology Based on Modified SWAT

896 Hydrological Modeling in Southwest Karst Area, China University of Geoscience,

897 Wuhan, China, 2006.

898 Shoemaker, W.B., Cunningham, K.J., and Kuniansky, E.L.: Effects of turbulence on

899 hydraulic heads and parameter sensitivities in preferential groundwater flow layers.

900   Water Resources Research, 44, 34-50. doi: 10.1029/2007WR006601, 2008.

901   Suo, L.T., Wan, J.W., and Lu, X.W.: Improvement and application of TOPMODEL in karst
902   region. Carsologica Sinica, 26(1), 67-70, 2007.

903   Williams, P. W.: Book Review: Methods in Karst Hydrogeology, Nico Goldscheider and
904   David Drew (eds). Hydrogeology Journal, 17,1025-1025, 2009.

905   Worthington, S., Ford, D., and Beddows, P.: Porosity and permeability enhancement in
906   unconfined carbonate aquifers as a result of solution. Speleogenesis: evolution of karst
907   aquifers, 2000.

908   Yang, P. H., Luo, J.Y., Peng, W., Xia, K.S., and Lin, Y.S.: Application of online technique in
909   tracer test-A case in Qingmuguan subterranean river system, Chongqing, China.
910   CARSOLOGICA SINICA, 27(3),215-220, 2008.

911   Yu, D., Yin, J., Wilby, R.L., Stuart, N. L., Jeroen, C., Lin, N., Liu, M., Yuan, H., Chen, J.,
912   Christel, P., Guan, M., Avinoam, B., Charlie, W. D., Tang, X., Yu, L., and Xu, S.:
913   Disruption of emergency response to vulnerable populations during floods. Nature
914   Sustainability, 3, 728–736. https://doi.org/10.1038/s41893-020-0516-7, 2020.

915   Yu, Q., Yang, P.H., Yu, Z.L., Chen, X.B., and Wu, H.: Dominant factors controlling
916   hydrochemical variationg of karst underground river in different period,
917   Qingmuguan,Chongqing. CARSOLOGICA SINICA, 35(2),134-143, 2016.

918   Zhang, Q.: Assesment on the intrinsic vulnerability of karst groundwater source in the
919   Qingmuguan karst valley. CARSOLOGICA SINICA, 31(1),67-73, 2012.

920   Zhu, C., and Li, Y.: Long-Term Hydrological Impacts of Land Use/Land Cover Change
921   From 1984 to 2010 in the Little River Basin, Tennessee. International Soil and Water
922   Conservation Research, 2(2), 11-21, 2014.

923

924 **Tables**

925   Table 1 Parameters of the QMG model.

Parameters	Variable name	Physical property
Infiltration coefficient	I_c	Meteorology
Evaporation coefficient	λ	Vegetation cover
Soil thickness	h	Karst aquifer
Soil coefficient	S_b	Soil type
Saturated water content	S_c	Soil type
Rock porosity	R_p	Karst aquifer
Field capacity	F_c	Soil type
Permeability coefficient	K	Karst aquifer
Flow direction	F_d	Landform
Slope	S_0	Landform
Specific yield	S_y	Karst aquifer
Channel roughness	n	Landform

926   Table 2 Parametric sensitivity results in QMG model.

Infiltration coefficient/I_c	Evaporation coefficient/λ	Thickness/h	Soil coefficient/S_b	Saturated water content/S_c	Specific yield/S_y
0.92	0.24	0.71	0.58	0.8	0.83

Flow direction/F_d	Slope/S_0	Rock porosity/R_p	Field capacity/F_c	Permeability coefficient/K	Channel roughness/n
0.74	0.68	0.86	0.78	0.89	0.36

927   Table 3 Flood simulation evaluation index through parametric optimization.

Parameter optimization	Parameter types	Nash coefficient	Correlation coefficient	Relative flow process error/%	Flood peak error/%	Water balance coefficient	Peak time error (hours)
calibration periods	initial	0.82	0.77	24	29	0.82	4
	optimized	0.91	0.94	14	12	0.95	2
validation periods	initial	0.79	0.71	29	32	0.77	6
	optimized	0.88	0.87	18	16	0.92	3
average value	initial	0.81	0.74	27	31	0.80	5
	optimized	0.90	0.91	16	14	0.94	3

928   Table 4 Flood simulation indices for model validation.

Floods	Parameter types	Nash coefficient	Correlation coefficient	Relative flow process error/%	Flood peak error/%	Water balance coefficient	Peak time error/ (hours)
2017042408	initial	0.77	0.7	28	29	0.71	-5
	optimized	0.95	0.89	11	15	0.88	-2
2017050816	initial	0.78	0.71	19	19	0.76	-4
	optimized	0.92	0.88	11	9	0.94	-2
2017061518	initial	0.76	0.6	25	32	0.63	-5
	optimized	0.91	0.93	12	11	0.95	-3
2017071015	initial	0.78	0.82	25	37	0.64	-4
	optimized	0.92	0.87	8	7	0.94	-2
2017091512	initial	0.81	0.62	21	16	0.78	-5
	optimized	0.9	0.92	13	10	0.9	-4
2017100815	initial	0.75	0.68	30	26	0.62	-2
	optimized	0.94	0.86	11	15	0.92	-1
2018052016	initial	0.78	0.68	25	21	0.67	5
	optimized	0.91	0.93	10	13	0.94	2
2018060815	initial	0.82	0.79	27	22	0.69	-6
	optimized	0.9	0.92	11	12	0.93	-4
2018071212	initial	0.84	0.75	26	24	0.61	5
	optimized	0.91	0.88	8	15	0.92	3
2018081512	initial	0.71	0.78	26	24	0.78	-4
	optimized	0.89	0.94	12	11	0.89	-3
2018090516	initial	0.85	0.68	28	23	0.68	-5
	optimized	0.93	0.87	12	10	0.92	-2
2018092514	initial	0.79	0.78	23	19	0.59	5
	optimized	0.88	0.88	9	11	0.89	2
2018101208	initial	0.78	0.81	28	25	0.63	5
	optimized	0.92	0.94	11	10	0.94	2
2018111208	initial	0.79	0.81	25	24	0.65	-6
	optimized	0.94	0.86	13	12	0.92	-2
2019042512	initial	0.78	0.8	26	36	0.8	5
	optimized	0.89	0.94	9	16	0.93	2
2019051513	initial	0.84	0.77	32	27	0.79	4
	optimized	0.91	0.88	9	13	0.95	2
2019052516	initial	0.74	0.75	29	26	0.63	-5
	optimized	0.92	0.86	7	15	0.96	-2
2019060518	initial	0.85	0.83	28	25	0.78	-4
	optimized	0.95	0.96	10	12	0.92	-2
average value	initial	0.79	0.74	26	25	0.69	5
	optimized	0.92	0.9	10	11	0.92	2

929   **Figures**
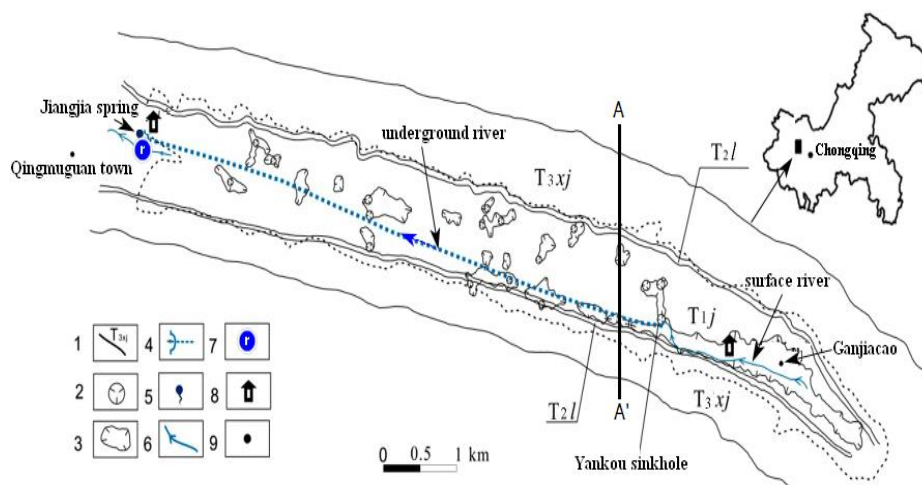
930

931   1- stratigraphic boundary, 2-sinkhole, 3- karst depression, 4- underground river, 5-
932   karst spring, 6-surface river，7-river gauge, 8- rain gauge, and 9- geographical name
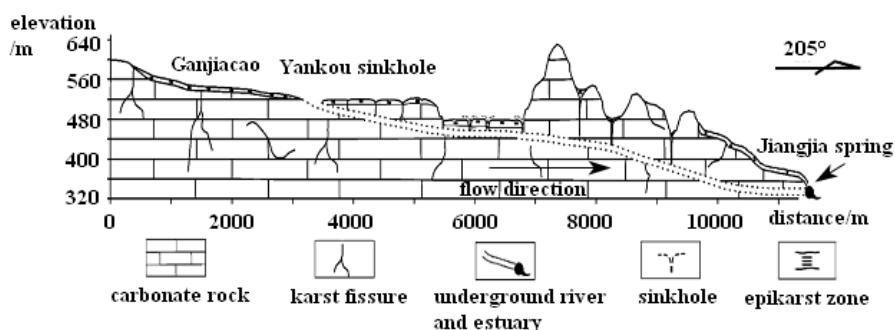933   a.   Qingmuguan karst basin (modified from Yu et al.,2016)
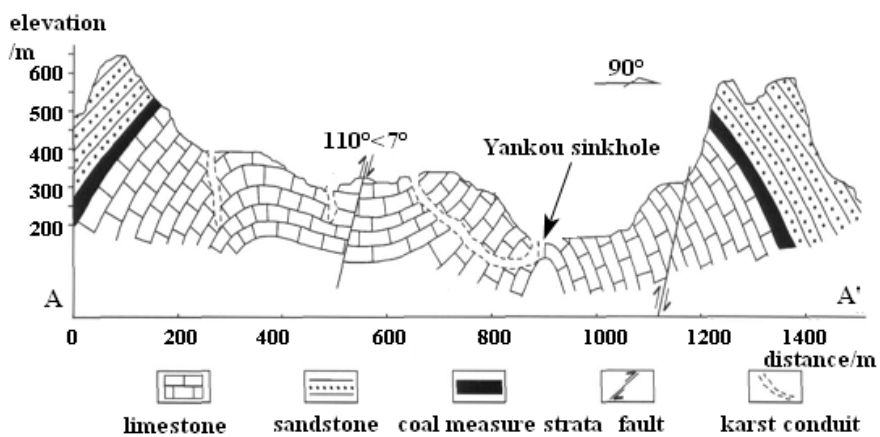
934

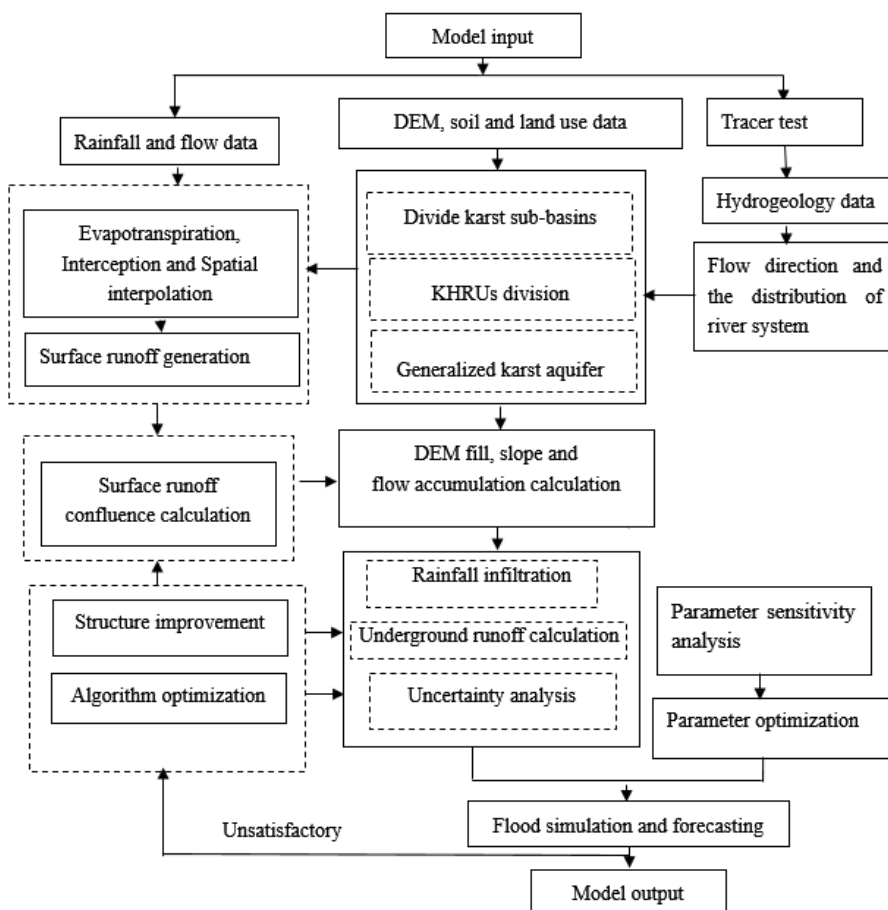935   b. Lithologic cross section of Yankou sinkhole/AA'(modified from Zhang,2012)

936

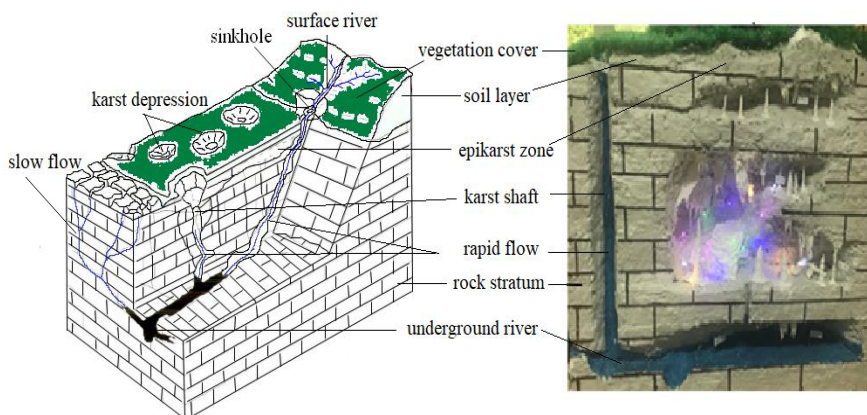937   c. Longitudinal profile of the study area (modified from Yang et al.,2008)

938   Figure 1 The Qingmuguan karst basin.

939

940   Figure 2 Modeling flow chart of QMG (Qingmuguan) model.

941

942   Figure 3 Spatial structure of the KHRUs (Li et al.,2021).
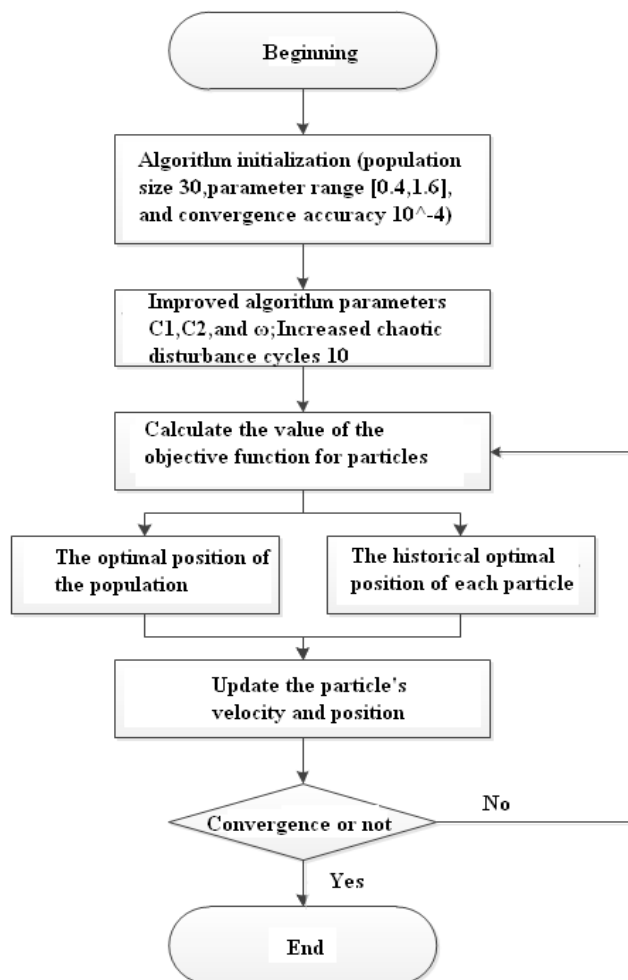
943

944 Figure 4 Algorithm flow chart of the IPSO.
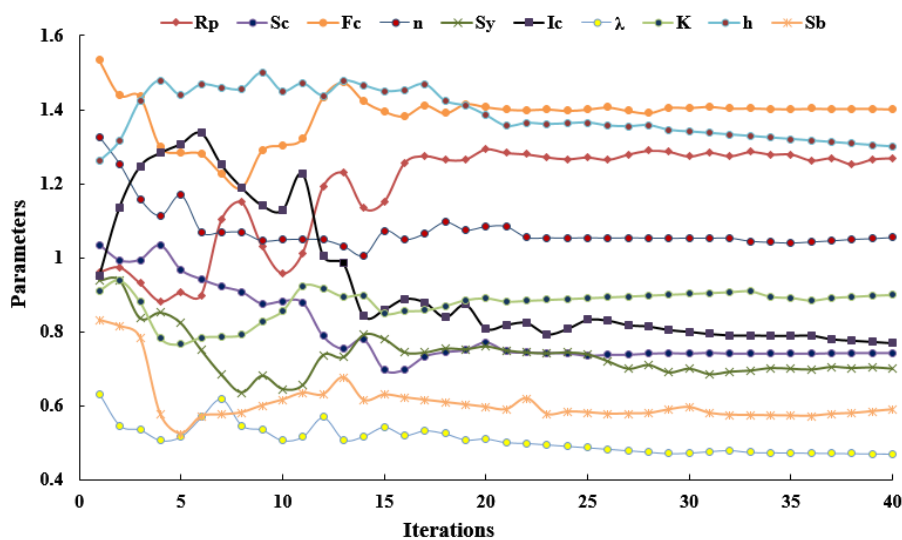
945

946 Figure 5 Iteration process of parametric optimization.
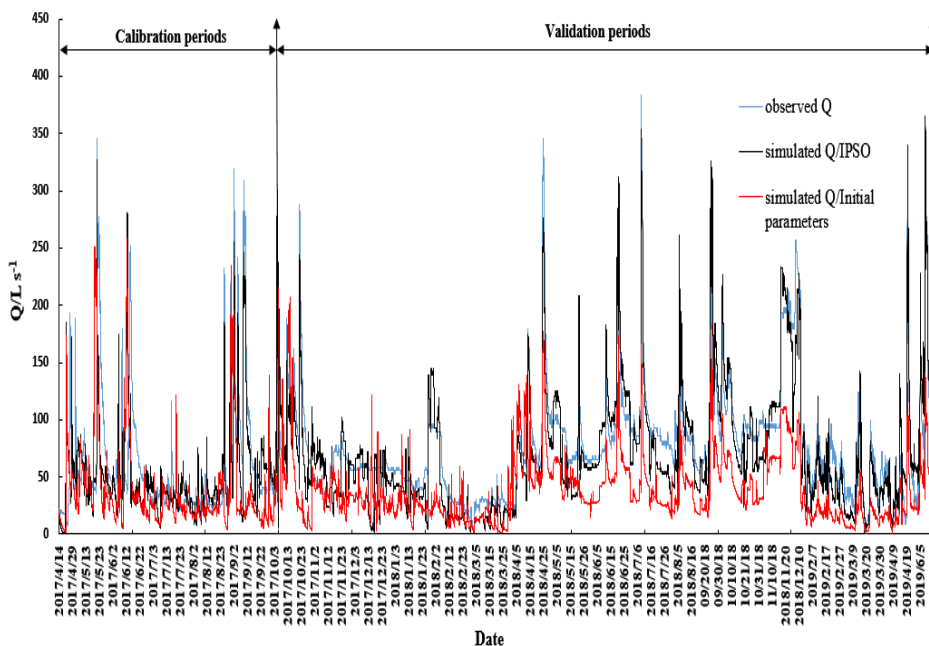
947

948 Figure 6 Flow simulation results of QMG model based on parameter optimization.
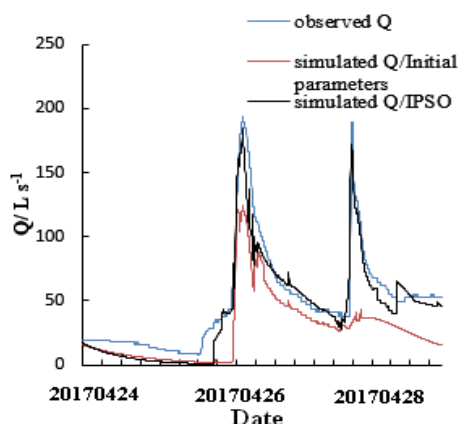
949

950   a. flood 201704240800   b. flood 201705081600
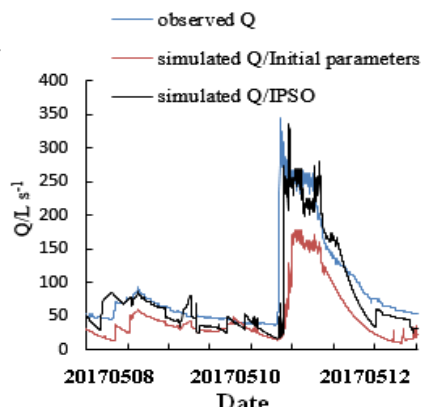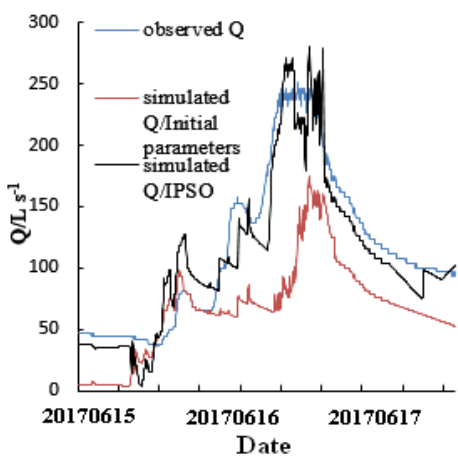
951

952   c.flood 201706151800   d. flood 201707101530
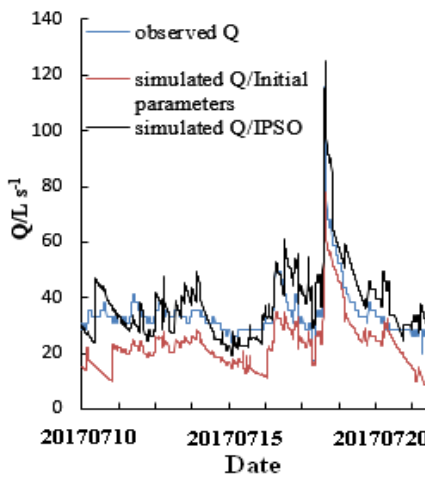
953
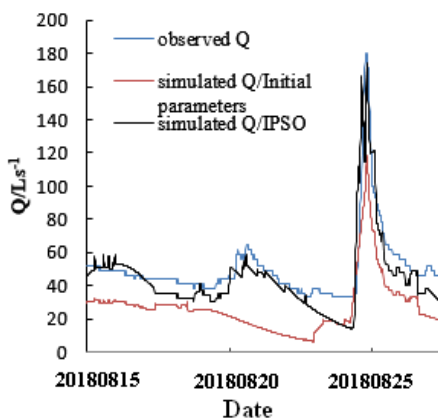
43

954
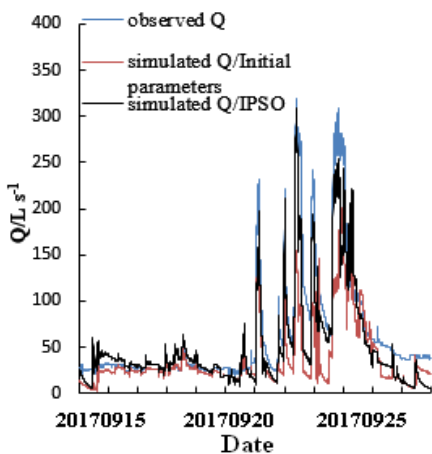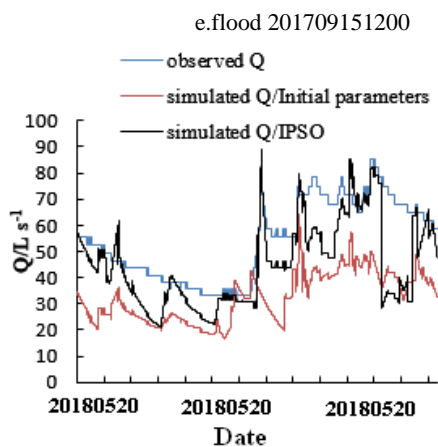
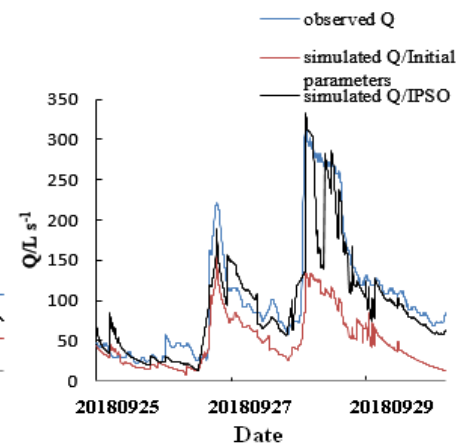e.flood 201709151200 f.flood 201710081500
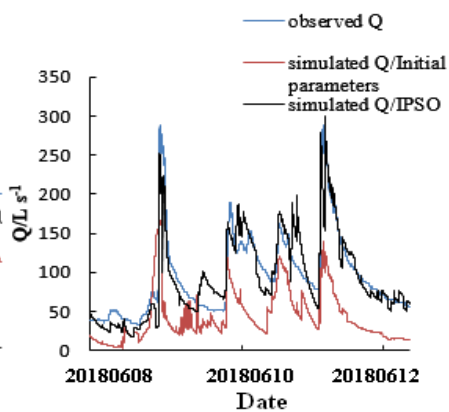
955

956

g.flood 201805201600 h.flood 201806081500

957

958 i.flood 201808151200 j.flood 201905251600

959 Figure 7 Flood simulation effects based on initial and optimized parameters.